FoMR
Frontiers of Multidisciplinary Research

Vol. 1 | No. 2 | Apr - Jun 2026

Comparative Study of Thermoelectric Performance in InP_3 and SnP_3 Monolayers: Role of Electronic Structure and Lattice Dynamics

Tanu Choudhary[a], Raju K Biswas[b*]

ABSTRACT

We conduct a detailed comparative investigation of the structural, electronic and thermal transport properties of monolayer InP_3 and SnP_3 based on first-principles calculations combined with Boltzmann transport theory. Both systems exhibit indirect semiconducting behaviour, however, their distinct electronic dispersion led to markedly different transport responses. InP_3 displays a pronounced DOS enhancement near the valence band maximum, which yields a larger Seebeck coefficient, thereby favouring *p*-type thermoelectric performance. Conversely, SnP_3 shows a higher DOS near the conduction band edge and intrinsically larger carrier concentration, resulting in significantly enhanced electrical conductivity. Additionally, notable phonon softening and bonding heterogeneity in SnP_3 suppress the lattice thermal conductivity, further improving thermoelectric efficiency. As a result, SnP_3 achieves a superior *p*-type figure of merit, reaching ZT ≈ 0.74 at 600 K, whereas InP_3 exhibits comparatively improved *n*-type performance due to its higher Seebeck coefficient. These results highlight the role of band-edge DOS engineering and phonon softening in optimizing thermoelectric behaviour in two-dimensional triphosphides.

Received date: 24.11.2025
Accepted date: 20.01.2026

Keywords: First-principles study, Thermoelectric, Density functional theory, Phosphides, Boltzmann transport theory

https://doi.org/10.65601/FoMR.2026.1.2.2

[a]*Department of Physics,*
Faculty of Natural Sciences,
M S Ramaiah University of Applied Sciences,
Bengaluru 560058, India

***Corresponding Author:**
[b]*Department of Physics,*
North Eastern Regional Institute of Science and Technology,
Nirjuli, Arunachal Pradesh, 791109, India
rajukumar1718@gmail.com

INTRODUCTION

Two-dimensional (2D) triphosphides have recently emerged as a promising family of layered materials with distinct structural and electronic characteristics. These compounds consist of phosphorus combined with selected group III, IV, or V elements and can be mechanically or chemically exfoliated from their van der Waals-bonded bulk counterparts. In the monolayer limit, triphosphides adopt a graphene-like topology with a robust hexagonal framework and typically exhibit an indirect band gap, making them suitable candidates for next-generation electronic and optoelectronic applications. First-principles studies have demonstrated that several members of this class including monolayer InP_3, GaP_3, SbP_3, and SnP_3 are dynamically and thermally stable (Gullman & Olofsson, 1972; Sun et al., 2020). Owing to their unique combination of structural stability, tuneable band gaps, and favourable carrier transport characteristics, 2D triphosphides have been widely proposed for applications in nanoelectronics, optoelectronics, field-effect transistors, and high-performance lithium-ion batteries.

Among the family, Indium triphosphide (InP_3) was first synthesized in the early 1980s under high-pressure conditions and subsequently quenched to ambient pressure (Kinomura et al., 1983). Bulk InP_3 crystallizes in a metallic phase with $R\bar{3}m$ symmetry, adopting a structure analogous to that of SnP_3. More recently, a two-dimensional monolayer of InP_3 with a graphene-like topology (G-InP_3) has been theoretically predicted through exfoliation of the layered bulk material (Miao et al., 2017). In contrast to its metallic bulk counterpart, monolayer G-InP_3 is predicted to be an indirect bandgap semiconductor with high and nearly isotropic electron mobility, suggesting strong potential for electronic and optoelectronic device applications (Liu et al., 2018; Yi et al., 2019). Furthermore, first-principles studies indicate that G-InP_3 exhibits favourable adsorption energetics and ion diffusion characteristics, making it a promising reversible anode material for ultrafast lithium- and sodium-ion storage (Liu et al., 2018; Zhang et al., 2018). Additional reports also propose its utility as a multifunctional material combining photovoltaic and thermoelectric characteristics at the same time (Sun et al., 2020).

Similar to InP_3, monolayer SnP_3 has also attracted considerable attention due to its rich optoelectronic and catalytic behaviour. Ghosh *et al*. demonstrated that monolayer SnP_3 exhibits a remarkably high optical absorption coefficient and favourable carrier mobility, underscoring its potential for next-generation optoelectronic devices (Ghosh et al., 2018). Wu *et al*. further reported that single-layer SnP_3 possesses excellent catalytic activity toward the hydrogen evolution reaction, identifying it as an efficient, metal-free electrocatalyst (Wu et al., 2019). Collectively, these findings suggest that 2D triphosphides combine high carrier mobility with chemically active surfaces, making them strong candidates for multifunctional applications.

In the context of thermoelectric, Zhang et al. conducted a comprehensive first-principles investigation of monolayer InP_3, GaP_3, SbP_3, and SnP_3, revealing that these materials possess intrinsically low lattice thermal conductivity and high thermoelectric performance driven by their favourable electronic transport characteristics (Sun et al., 2020). More recently, Zhu et al. identified SnP_3 as an outstanding *p*-type thermoelectric material, with a power factor and figure of merit comparable to or exceeding those of many 2D thermoelectrics (Zhu et al., 2019). Together, these results point to the significant potential of triphosphide monolayers for advanced thermal-management and energy-conversion application.

Despite these encouraging predictions, the transport and thermoelectric properties of 2D triphosphides remain insufficiently explored. In particular, comprehensive studies of heat transport and the underlying phonon mechanisms in key members such as SnP_3 and InP_3 are still lacking. This gap motivates the present work, which aims to provide a detailed understanding of their transport behaviour for future thermoelectric applications.

Herein, we combine first-principles density functional theory with the phonon Boltzmann transport equation to conduct a comprehensive comparative investigation of the transport and thermoelectric properties of monolayer InP_3 and SnP_3. We examine their lattice structures, phonon dispersion relations, and lattice thermal conductivity, revealing phonon softening and reduced group velocities in SnP_3

strongly suppress its κ_{latt}. We further analyse the electronic band structures and evaluate carrier mobilities via the deformation potential framework. Finally, by computing the Seebeck coefficient, electrical conductivity, and thermoelectric figure of merit (ZT), we demonstrate that both triphosphides display promising thermoelectric performance, with distinct advantages arising from their differing electronic and phononic characteristics. This work provides crucial insight into the transport behavior of 2D triphosphides and establishes InP_3 and SnP_3 as strong contenders for thermoelectric applications.

COMPUTATIONAL DETAILS

First-principles simulations were carried out within the framework of density functional theory (DFT) using the Quantum Espresso (QE) package (Giannozzi et al., 2009). The Perdew-Burke-Ernzerhof (PBE) (Perdew et al., 1992) functional using the generalized gradient approximation (GGA) (Perdew et al., 1996) technique was employed to describe the exchange-correlation interactions in all calculations performed using the QE package. For structural optimization, a kinetic energy cutoff of 60 Ry was used for the wave functions, while a cutoff of 240 Ry was applied to the charge density. The lattice parameters were fully optimized, and atomic positions were relaxed until the total energy convergence threshold reached 10^{-10} Ry. For self-consistent field (SCF) calculations, a 20 x 20 x 1 Monkhorst-Pack (Wang et al., 2021) k-point grid is employed. We have obtained phonon dispersion using density functional perturbation theory (DFPT) (Baroni et al., 2001) along the q-point with 4 x 4 x 1 q-mesh in the Brillouin zone. To investigate the bonding characteristics, crystal orbital Hamilton population (COHP) (Deringer et al., 2011) analysis was performed using the LOBSTER code (Maintz et al., 2016) to provide insights into the electronic structure-derived bonding interactions.

The electronic transport properties are obtained using semiclassical Boltzmann transport theory within the rigid band approach and constant relaxation-time approximation (RTA) as implemented in the BoltzTraP code (Madsen & Singh, 2006). The constant scattering time approximation is employed, under the condition that, the scattering time exhibits negligible variation with energy on a scale of k_BT. The BoltzTraP code effectively solves the Boltzmann equation through band structure interpolation and the execution of all requisite integration procedures. To conduct the Fourier interpolation of the Kohn-Sham eigenvalues, we utilized a dense 24 x 24 x 1 k-mesh across the Brillouin zone (BZ). The Seebeck coefficient (S), also known as thermoelectric power, is obtained as (Madsen & Singh, 2006),

$$S_{\alpha\beta}(T,\mu) = \frac{1}{eT\Omega\sigma_{\alpha\beta}(T,\mu)} \int \sigma_{\alpha\beta}(\varepsilon)(\varepsilon-\mu)\left[-\frac{\delta f_0(T,\varepsilon,\mu)}{\delta\varepsilon}\right]d\varepsilon \quad (1)$$

Here, $\sigma_{\alpha\beta}$ are the transport distribution tensor elements calculated using the Fourier interpolation of the band structure. α and β are the tensor indices. Ω, μ, f_0, and T are the cell volume, chemical potential, Fermi distribution function, and absolute temperature, respectively.

RESULTS AND DISCUSSION

Crystal structure

The monolayer triphosphides InP_3 and SnP_3 crystallize in a trigonal structure with $R\bar{3}m$ space group symmetry, consistent with previous reports on layered metal phosphides (Sun et al., 2018). The primitive cell comprises six phosphorus atoms and two metal atoms arranged in a trigonal lattice (Fig. 1). Within the layer, the P atoms form slightly distorted hexagonal rings. These P-hexagons are interconnected via the incorporated metal atoms, leading to a network in which the metal sublattice itself forms a larger hexagonal arrangement. The optimized in-plane lattice parameters are $a = b = 7.51$ Å for InP_3 and 7.45 Å for SnP_3, with an out of plane parameter c ≈ 15.65 Å, in excellent agreement with earlier experimental and theoretical data (Gullman & Olofsson, 1972; Zhu et al., 2019). The local bonding environment exhibits subtle differences between the two compounds. In InP_3, the P-P and In-P bond lengths are 2.56 Å and 2.23 Å, respectively, whereas, SnP_3 displays slightly elongated P-P bonds (2.76 Å) and shorter Sn-P bonds (2.13 Å). This contrast suggests comparatively stronger Sn-P orbital hybridization and a relatively more expanded P network in SnP_3. Such structural variations are expected to modulate the electronic properties, charge transfer characteristics, and lattice dynamical behaviour, thereby giving rise to distinct electronic and phononic transport properties in the monolayer systems.

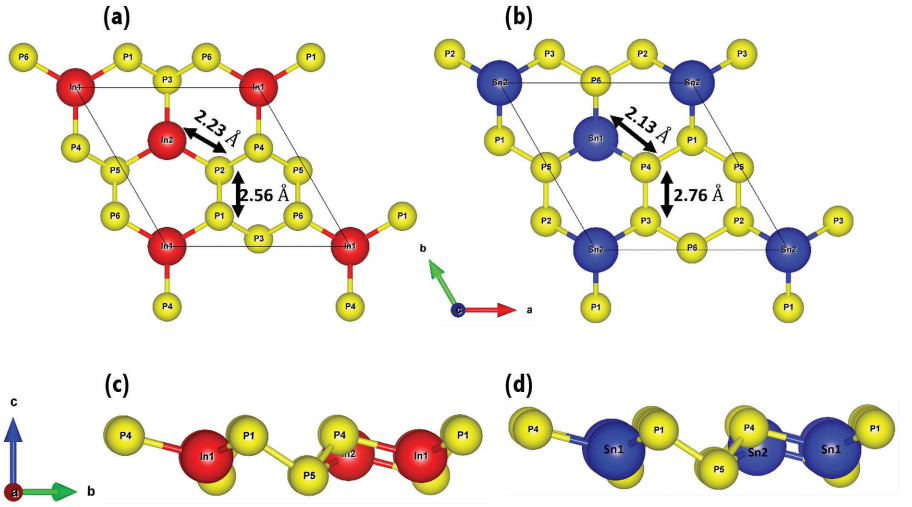

Figure 1 Schematic illustration of the (a) top view and (c) side view of InP_3 structure and (b) top view (d) side view of SnP_3. The corresponding bond lengths are also indicated.

Electronic properties

To gain insight into the electronic characteristics of monolayer InP_3 and SnP_3, we computed their electronic band structures along the high-symmetry path Γ–M–K–Γ in the Brillouin zone, together with the total and projected density of states (DOS and PDOS), as shown in Figure 2. Both systems exhibit semiconducting behaviour, with indirect band gaps of 0.80 eV for InP_3 and 0.60 eV for SnP_3 as shown in figure 2a and 2b, respectively. In SnP_3, the conduction band minimum (CBM) is located at the Γ point while the valence band maximum (VBM) occurs at the M point, indicating an indirect Γ–M transition. In contrast, InP_3 shows an indirect gap with VBM lies along the Γ–M path, reflecting a slightly different band dispersion near the Fermi level. These variations in band-edge positions originate from the distinct bonding environments in the two monolayers.

The PDOS analysis provides deeper insight into the orbital contributions. As illustrated in Figure 2c and 2d, the VBM is predominantly dominated by P-3p orbital in both compounds, indicating that the valence states originate mainly from the P atoms. Meanwhile, the CBM shows stronger contributions from the metal cation orbitals (In-5p for InP_3 and Sn-5p for SnP_3), with some contribution coming from 3p states of P atoms. The PDOS plots further confirms that the VBM is largely localized on the P hexagonal rings, while the CBM exhibits localization around the metal sites with weaker extension toward neighbouring P atoms.

The total DOS (Figure 2e) reveals that SnP_3 exhibits a higher DOS near the CBM, while InP_3 shows comparatively higher DOS near the VBM. A higher DOS near the Fermi level generally enhances the energy-dependent carrier transport coefficients, particularly the Seebeck coefficient. Thus, the large DOS near the VBM in InP_3 suggests the potential for enhanced *p*-type thermoelectric performance, while the increased DOS near the CBM in SnP_3 implies that it may exhibit favourable *n*-type Seebeck response. These distinctions highlight how intrinsic electronic structure, chemical bonding, and orbital hybridization collectively govern the electronic and thermoelectric behaviour of the two monolayer systems.

Crystal orbital Hamilton population (COHP) and charge density

The crystal orbital Hamilton population (COHP) analysis, shown in Figure 3a and 3b, provides a quantitative assessment of bonding interactions in the InP_3 and SnP_3 monolayer by distinguishing bonding and anti-bonding contributions as a function of energy relative to the Fermi level (E_F). Positive COHP values represent anti-bonding states and negative values correspond to bonding character. For both materials, the P-P bonds display predominantly bonding states below the Fermi level, indicating stable covalent interactions within the phosphorus hexagonal ring. In contrast, the metal-P bonds (In-P in InP_3 and Sn-P in SnP_3) exhibit significant antibonding contributions near the Fermi level, which suggests weaker metal-P interactions

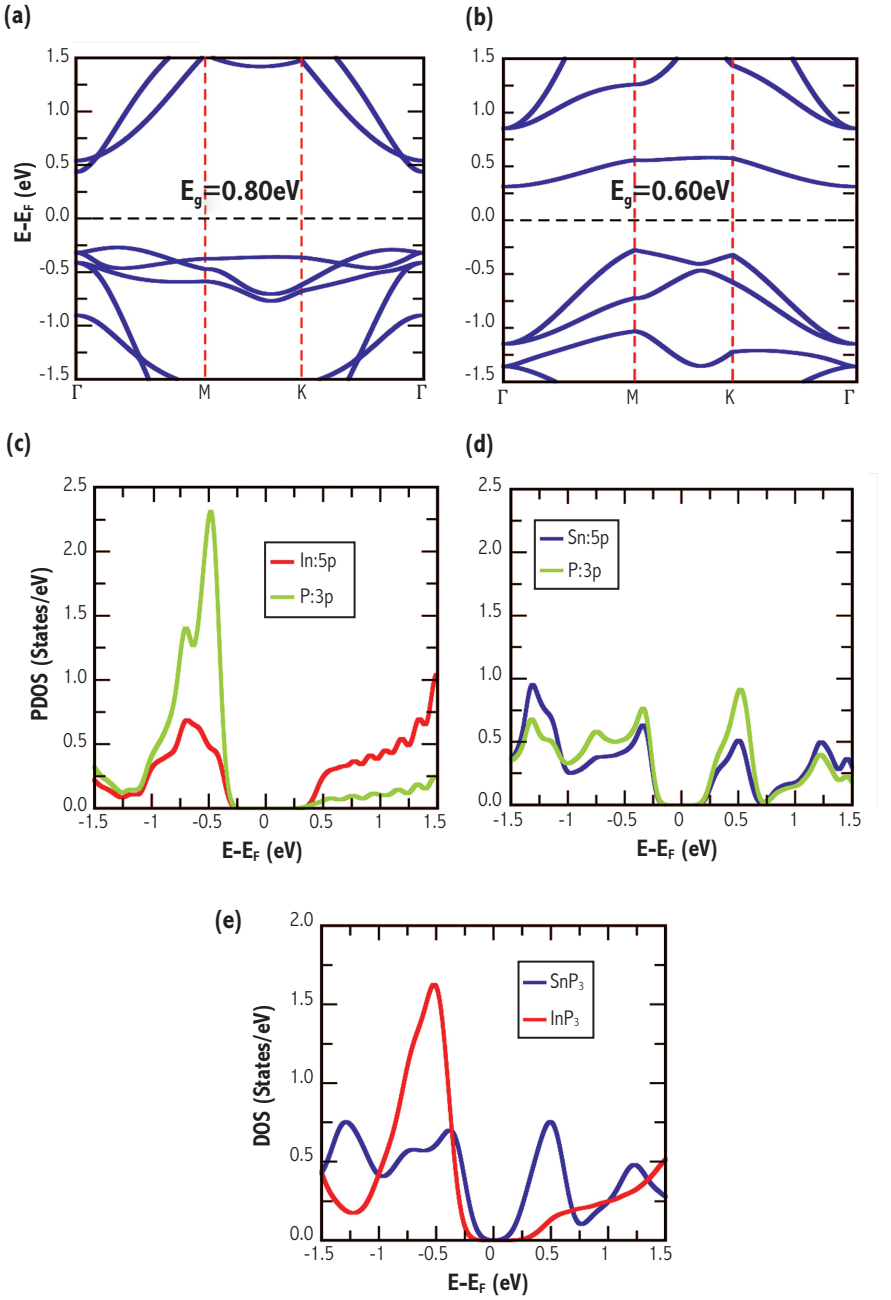

Figure 2 The electronic band structure of (a) InP_3 and (b) SnP_3 along the high-symmetric points in the irreducible Brillouin zone. The band gap (E_g) of the system is mentioned in black colour text. Calculated projected density of states (PDOS) for (c) InP_3 and (d) SnP_3. (e) Total density of states (DOS) for both the monolayer systems.

compared to the P-P framework. These antibonding characteristics reduce the bond stiffness associated with metal-P bonds, resulting in lower average force constants. Such a reduction in bond stiffness leads to lower phonon group velocities and enhanced phonon scattering, which collectively contribute to the suppressed lattice thermal conductivity (κ_{latt}) observed in these monolayers.

Consistent with the COHP results, the charge density distribution (Figures 3d and 3e) shows that the P-P bonds exhibit strong charge overlap, confirming their covalent and structurally integrated

nature. In contrast, the charge density between the metal atoms and adjacent phosphorus atoms is more localized and asymmetric, indicating weaker interactions in the metal-P network. This spatial localization correlates closely with the antibonding COHP signatures, reinforcing that the metal-P bonds are weaker than the P-P bonds. The coexistence of strong P-P bonding within the ring and weaker metal-P connections form a bonding heterogeneity (Dutta et al., 2019), which is known to induce phonon coupling mismatch and enhanced phonon scattering, further reducing κ_{latt}.

Following the charge density analysis, we further employed the Bader charge analysis to probe the electronic environment of monolayer InP_3 and SnP_3. Bader charge analysis provides vital insight into

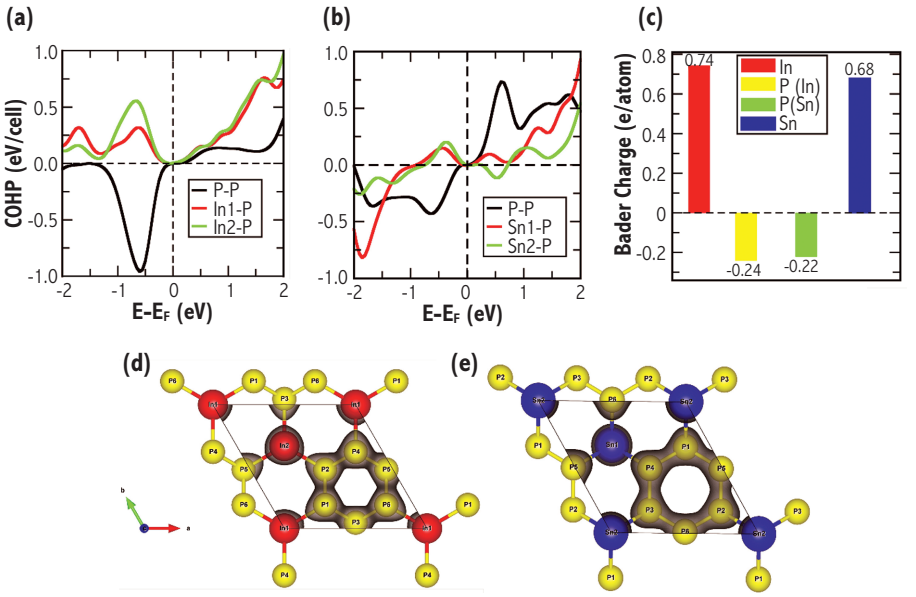

Figure 3 Crystal orbital Hamilton population (COHP) plot as a function of energy (E) to discern bonding characteristics between different pairs of ions for (a) InP_3 and (b) SnP_3. Here, the positive value of (COHP) signifies orbital overlapping between two ions that are antibonding in nature, whereas negative values correspond to bonding interactions. (c) Bader charge analysis for both the systems. Top view of charge densities calculated with DFT visualized at the isosurface value of 0.065 eÅ^{-3} for (d) InP_3 and (e) SnP_3.

the charge redistribution among ions and helps to quantify the degree of charge transfer in a system, offering a deeper understanding of chemical bonding. The degree of charge transfer inferred from Bader charges is often used to assess the ionic or covalent character of bonding. Specifically, if the Bader charge of an atom closely approaches its formal oxidation state, it indicates a predominantly ionic interaction, reflecting substantial electron transfer. Conversely, significantly lower Bader charges suggest a higher degree of covalent character due to shared electron density between ions. The Bader charge analysis (Figure 3c) supports this bonding interpretation by quantifying the charge transfer between atoms. In InP_3, the Indium atoms donate approximately 0.74 |e|, while in SnP_3, the Sn atoms donate around 0.68 |e| to the surrounding P atoms. The phosphorus atoms receiving negative charge indicate their role as electron acceptors, while the metal atoms act as electron donors. This charge redistribution confirms the presence of mixed bonding character, where the P-P bonds remain predominantly covalent, while the metal-P bonds exhibit partial ionic nature. Compared to nominal valence states, the observed charge transfer is moderate, highlighting that neither structure is purely ionic nor purely covalent, but instead stabilized through covalent P-P frameworks bridged by partially ionic metal-P linkages. This mixed bonding nature directly contributes to the soft lattice dynamics and inherently low lattice thermal conductivity in both monolayers.

Carrier transport properties

To quantitatively evaluate the carrier transport of the designed systems, we employed the deformation potential theory (DPT) (Shuai et al., 2012), which

describes the longitudinal acoustic (LA) phonon-limited mobility arising from carrier scattering due to lattice deformations induced by long-wavelength acoustic phonons. Based on the principles of Boltzmann transport theory, the mobility of charge carriers, $\mu_{LA}^{(e/h)}$ (electrons/holes) can be expressed as (Shuai et al., 2012),

$$\mu_{LA}^{(e/h)} = \frac{C_{2D}\hbar^3 e}{E_1^2 (m^*)^2 k_B T} \quad (2)$$

Where, e is the charge of electron, $\hbar$ is the reduced Planck constant, k_B is the Boltzmann constant, T is the temperature, m^* is the effective mass of charge carriers (electrons and holes) and E_1 represents the deformation potential constant or the carrier-phonon scattering strength defined by, $E_1 = \frac{\Delta E_{Band}}{(\Delta a/a_0)}$. Here, ΔE_{Band} is shift in energy level at the band edge position because of uniaxial strain, $\Delta a/a_0$. Here, a_0 is the initial lattice parameter, Δa denotes the change in lattice parameter caused by the applied uniaxial strain. C_{2D} is the elastic constant determined by fitting the energy-strain curve to quadratic polynomial. The carrier effective mass (m^*) is obtained by parabolic fitting of the band edges in the E-k dispersion. A steeper band curvature yields a smaller m^*, while a flatter band gives a larger m^*. Carrier effective mass (m^*) is determined using the equation (Gorczyca, et al., 2008),

$$m^* = \hbar^2 \left[\frac{d^2 E_k}{dk^2}\right]^{-1} \quad (3)$$

Within the framework of Boltzmann transport theory, the carrier mobility (μ) is governed by the interplay of three key parameters: the elastic constant (C_{2D}), the deformation potential constant (E_1), and the effective carrier mass (m^*), as expressed in equation (3). A lower deformation potential indicates weaker scattering of charge carriers by lattice vibrations, whereas a higher elastic modulus reflects a mechanically stiffer lattice capable of supporting efficient carrier transport. Additionally, a smaller effective mass is directly associated with higher carrier mobility, as carriers can respond more readily to an applied electric field. Notably, all calculated parameters reported here are consistent with previously reported theoretical results for these compounds, confirming the reliability of our computational approach (Yi et al., 2019; Saeed et al., 2017; Zhu et al., 2019). The calculated values for elastic constants, deformation potential constants and mobility of electrons and holes are summarized in Table 1.

As shown in figure 4b, InP_3 exhibits significantly higher carrier mobility than SnP_3 for both electrons and holes. For electrons in InP_3, the effective mass is comparatively small (0.45 m_0) and the deformation potential is moderate (2.2 eV), while the material maintains a relatively high elastic modulus (52 N/m^2). These favourable conditions result in a high electron mobility of 1093 cm^2/Vs. In contrast, SnP_3 shows a larger electron effective mass (0.92 m_0) and a higher deformation potential (3.1 eV), along with a lower elastic modulus (34 N/m^2), leading to a much lower electron mobility of 156 cm^2/Vs. This trend is further visualized in the effective mass plot (Figure 4a) and the mobility comparison (Figure 4b), clearly showing that the larger carrier mass in SnP_3 hinders charge transport efficiency.

A similar trend is observed for hole carriers, for InP_3, holes possess a very low effective mass (0.32 m_0) with a deformation potential of (4.4 eV), resulting in a hole mobility of 546 cm^2/Vs. Meanwhile, SnP_3 exhibits heavier hole mass (0.81 m_0) and slightly lower deformation potential (2.3 eV), yielding a much lower hole mobility of 201 cm^2/Vs. The consistently lower charge carrier effective masses in InP_3 indicate steeper band dispersion near the band edges, corroborating its superior intrinsic transport performance. Notably, the calculated mobility values for both InP_3 and SnP_3 are in good agreement with previously reported theoretical results (Sun et al., 2020; Yi et al., 2019; Sun et al., 2018), validating the accuracy and reliability of our computational methodology.

Overall, the comparison clearly demonstrates that InP_3 offers more favourable electronic transport characteristics than SnP_3, primarily due to its lower effective charge carrier masses and higher lattice stiffness, which reduce phonon-induced scattering and enhance mobility. These properties suggest that InP_3 is more promising for applications requiring high carrier transport efficiency, such as nano-electronic and thermoelectric devices.

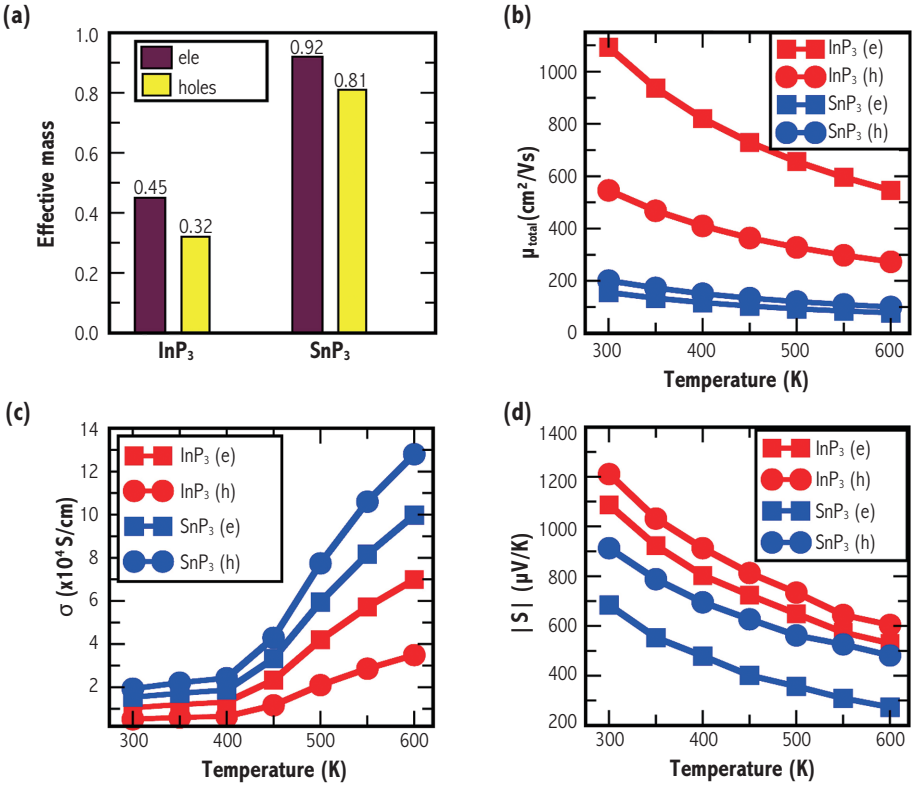

Figure 4 (a) Effective mass comparison for both the monolayer systems. The calculated (b) total mobility (c) electrical conductivity and (d) Seebeck coefficient for n- and p- type in monolayer systems as function of temperatures.

Table 1 Calculated values of deformation potential constant (E_1), elastic constant (C_{2D}), carrier effective mass (m^*), carrier mobility (μ). m_0: bare electron mass (9.1 x 10^{-31} Kg).

Materials		E_1 (eV)	C_{2D} (N/m²)	$m^*(m_0)$	Mobility (cm²/Vs)
InP_3 (Sun et al., 2020; Yi et al., 2019)	**electrons**	2.2	52	0.45	1093
	holes	4.4		0.32	546
SnP_3 (Sun et al., 2020; Zhu et al., 2019)	**electrons**	3.1	34	0.92	156
	holes	2.3		0.81	201

Electronic transport properties

Figure 4(c) present the temperature-dependent electrical conductivity ($\sigma=ne\mu$) of the both systems. For each system, the carrier concentration was optimized by simultaneously considering the Seebeck coefficient and carrier mobility to provide a reliable estimate of conductivity. Following earlier reports on related InP_3 and SnP_3, (Yi et al., 2019) a comparable carrier concentration range was adopted, and the optimized values for both n-type and p-type carriers were found to lie around 10^{13} to 10^{14} cm^{-3} for both the systems, consistent with previous theoretical studies (Sun et al., 2020; Yi et al., 2019; Jalil et al., 2020) We observe that the

σ of SnP_3 is significantly higher than that of InP_3 over the entire temperature range. This is mainly due to the higher carrier concentration *(n)* in SnP_3. Although the mobility of SnP_3 is lower compared to InP_3 (as discussed earlier), the larger carrier concentration compensates for this and results in an overall enhancement in σ. At 300 K, the electrical conductivity of SnP_3 is calculated to be ~1.93 x 10^4 S/cm. whereas InP_3 shows a comparatively lower value of ~1.05x10^4 S/cm. This trend becomes more pronounced at elevated temperatures, where thermally activated carriers further enhance σ in both materials.

The electronic transport properties of both systems were evaluated within the constant relaxation time approximation by solving the Boltzmann transport equation (BTE) as implemented in the BoltzTraP code (Madsen & Singh, 2006). The calculated Seebeck coefficients (S) in the temperature range 300-600 K are summarized in Figure 4(d). At 300 K, the InP_3 system exhibits a Seebeck coefficient of 1211 μV/K for electrons and 1087 μV/K for holes, significantly higher than the corresponding values of 913 μV/K and 684 μV/K observed in SnP_3. This pronounced enhancement in the In-based system is attributed to sharp peaks in the DOS near the Fermi level (see figure 2 (e)), enhances the density-of-states effective mass and strengthens the energy-dependent asymmetry in carrier transport, thereby amplifying the Seebeck coefficient. In contrast, the Sn-based system shows relatively smoother DOS features, resulting in lower Seebeck values across the temperature range. This behaviour originates from its significantly enhanced electrical conductivity, which more than compensates for the reduced Seebeck response.

Phonon dispersion

The dynamical stability of the InP_3 and SnP_3 monolayer is examined using density functional perturbation theory (DFPT), and the corresponding phonon dispersion relations is calculated along the Γ–M–K–Γ high-symmetry path of the Brillouin zone, as shown in figures 5(a) and (b), respectively. The absence of imaginary frequencies across the Brillouin zone confirm that both the structures are dynamically stable. For a unit cell containing N atoms, the phonon spectrum consists of 3N vibrational branches, of which three are acoustic and the remaining 3N-3 are optical modes. In the present case, with eight atoms in the conventional unit cell, the phonon spectra therefore comprise three acoustic branches and 21 optical branches. The acoustic modes include one longitudinal acoustic (LA), one transverse acoustic (TA), and one out-of-plane acoustic (ZA) branch, while the optical branches span a broad frequency window and can be categorized into low-, mid-, and high-frequency regions, corresponding to distinct atomic vibration patterns. The clear separation between acoustic and optical branches, together with the diversity of optical modes, highlights the complex lattice dynamics of these monolayer structures, which play a crucial role in governing phonon transport and thermal conductivity.

Figure 5(a) and (b) present the phonon dispersion relations of InP_3 and SnP_3, providing a detailed picture of how the change of metal atom modifies lattice dynamics. At the same time, several distinct spectral features emerge, which explain the suppression of lattice thermal conductivity (κ_{latt}) in these systems. A systematic softening of phonon modes is observed (figure 5 (b)), most prominently in the acoustic mode in the Sn-based system. This softening originates from the increased atomic mass of Sn relative to In and leads to reduced phonon group velocities, thereby weakening the heat-carrying capability of acoustic phonons.

Moreover, the Sn system exhibits the softening of the low frequency optical modes. Interestingly, we obtain the ZO mode frequency at zone centre as low as 21.39 cm^{-1}, which is notably lower compared to InP_3 i.e. 63 cm^{-1}. This variation in the ZO phonon mode can be ascribed to the weaker restoring forces arising from the heavier atomic mass and reduced bond stiffness in SnP_3 compared to InP_3. The presence of Sn, being heavier than In, lowers the vibrational energy scale and leads to softer optical branches. Such phonon softening generally enhances phonon-phonon scattering, thereby suppressing lattice thermal conductivity and improving the thermoelectric performance.

Furthermore, we assess the Debye temperature (θ_D), a key descriptor of lattice vibrational stiffness and closely linked to κ_{latt}. According to Slack's theory (Slack, 1973), a lower θ_D typically corresponds to lower κ_{latt}, as it implies reduced phonon velocities and lower acoustic phonon frequencies, which in turn enhance phonon populations and scattering

rates (Mohanta et al., 2020). The calculated Debye temperature values for both the systems are presented in Table 2. The Debye temperature follows the order InP_3 (~76.3 K) > SnP_3 (34.5 K), indicating that the Sn-based system has a lower θ_D, possesses softer lattice dynamics and higher phonon scattering, thereby contributing to its reduced κ_{latt}.

Table 2 Calculated values of Debye cut off frequency (cm^{-1}) and Debye temperature (θ_D).

Material	Debye cut-off frequency (cm^{-1})	Debye temperature, (θ_D) (K)
InP_3	53	76.3
SnP_3	24	34.5

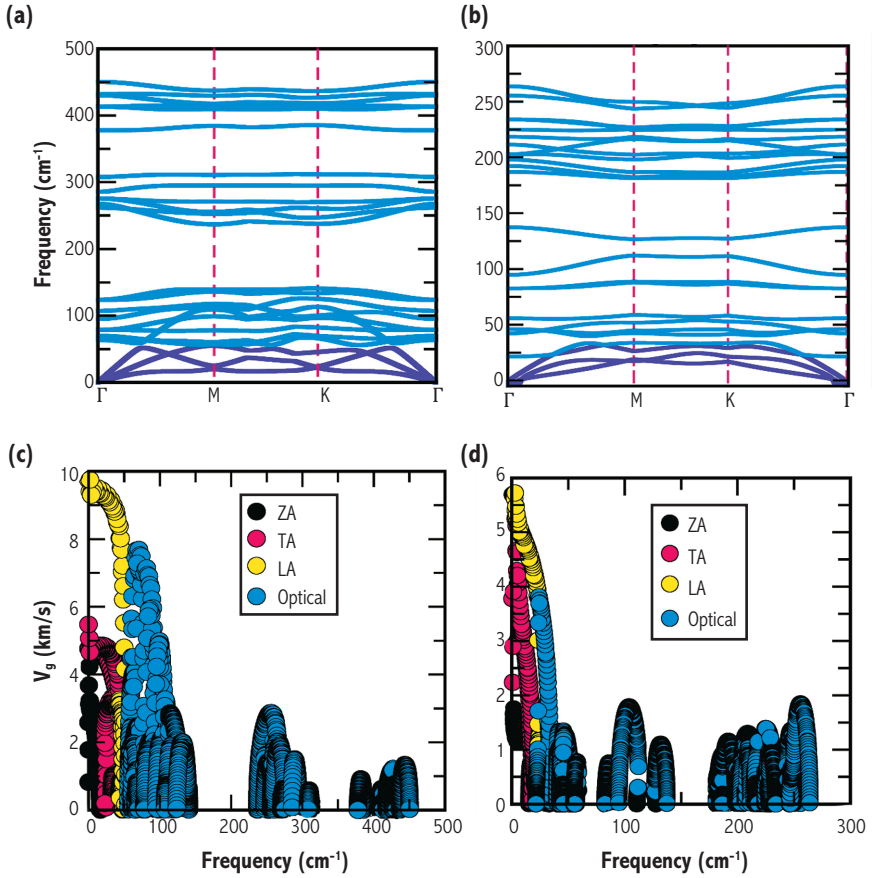

Figure 5 Phonon dispersion curves along the high-symmetry directions (Γ–M–K–Γ) of the BZ for (a) InP_3 and (b) SnP_3. The purple curves represent the acoustic phonon modes, blue curves indicate optical modes. The calculated group velocity of acoustic (ZA, TA, LA) and high frequency optical phonon (others) for (c) InP_3, (d) SnP_3.

To obtain the insight into the phonon transport properties and specify the role of each vibrational mode in determining low lattice thermal conductivity in InP_3 and SnP_3 systems, we compare the group velocity of both the monolayer systems. Phonon group velocity is defined as the derivative of the phonon frequency ω with respect to the wavevector q and reflects the rate at which vibrational energy propagates through the lattice, given by (Backman et al., 2024), $\nu_{\lambda,q} = \frac{\partial \omega_{\lambda,q}}{\partial q}$, where $\omega_{\lambda,q}$ denotes the phonon frequency. Figure 5 (c) and (d) illustrate the group velocity distribution of phonon modes for InP_3 and SnP_3 monolayer. Sn-based system exhibit clear phonon softening, evidenced by the overall reduction in group velocities compared to their counterparts, consistent with the heavier Sn atom incorporation that lowers acoustic as well as optical phonon dispersion. This feature makes the Sn-based system especially prone to low lattice thermal conductivity. Furthermore, optical phonon modes in Sn system exhibit markedly lower

group velocities than acoustic modes, with low-frequency optical branches displaying relatively higher values compared to mid- and high-frequency optical modes. The reduced group velocity across both acoustic and optical modes thus serves as a fundamental mechanism limiting thermal transport in these monolayer systems, highlighting the role of phonon softening in driving the suppression of κ_{latt}.

Lattice thermal conductivity and Figure of merit

We have employed the Slack model (Morelli et al., 2002), as explored in the previous studies (Jia et al., 2017), for expressing lattice thermal conductivity. Slack proposed an approach that accounts lattice thermal resistance arising solely from intrinsic phonon-phonon interactions, can be expressed as follows (Morelli et al., 2002).

$$\kappa_{latt} = \frac{A\, M_{av} \Theta^3 \delta}{\gamma^2 n^{2/3}\, T} \qquad (4)$$

Here, M_{av} is the average atom mass in atomic units, δ is the volume per atom in cubic angstroms, n is the number of atoms in the primitive cell and $A = \frac{2.43 \times 10^{-8}}{1 - \frac{0.514}{\gamma} + \frac{0.228}{\gamma^2}}$. Here the Θ, is calculated from its proportionality to the average velocity inside the crystal as (Morelli et al., 2002),

$$\Theta = \frac{h}{k_B}\left[\frac{3m}{4\pi}\right]^{1/3} n^{-1/3} v_a \qquad (5)$$

Here m is the number of atoms per volume and the corresponding averaged velocity, $v_a = \left[\frac{1}{3}\left(\frac{1}{v_{LA}^3} + \frac{1}{v_{TA}^3} + \frac{1}{v_{ZA}^3}\right)\right]^{-1/3}$, v_{LA}, v_{TA} and v_{ZA} are the group velocity of LA, TA and ZA modes. The Slack method emphasizes on acoustic phonons and approximates the lattice thermal conductivity by considering the average atomic mass, Grüneisen parameter, with the Debye temperature (Θ) computed based on the average group velocity of these acoustic modes. We obtain the κ_{latt} for temperatures ranging from 300 to 600 K as shown in Figure 6 (a). The calculated κ_{latt} value for InP_3 is 0.56 W/mK and 0.51 W/mK for SnP_3 at 300 K. The predominance of low group velocity arising from the phonon softening along with the low Debye temperature are responsible in reducing κ_{latt} in SnP_3 systems compare to InP_3. The values of κ_{latt} for both the materials are consistent with previously reported data (Sun et al., 2020), affirming the accuracy of the model for these materials.

Based on the computed electronic and phonon transport properties, the thermoelectric figure of merit (ZT) for the both monolayers are evaluated and depicted in Figures 6(b). The plot clearly illustrates that the ZT values reach a maximum for p - type (~0.74) at a higher temperature of 600 K for SnP_3 system. The increased ZT observed in the SnP_3 can be attributed to its relatively higher electrical conductivity and overall low lattice thermal conductivity. Furthermore, the elevated p-type figure of merit (ZT) value observed in SnP_3 system indicates the prevalent p-type nature of the material compared to its n-type counterpart. In comparison, InP_3 demonstrate moderately enhanced thermoelectric performance in the n-type regime, with ZT values of ~0.42 and ~0.27, respectively, at 600 K, which can be primarily attributed to their higher Seebeck coefficients. These observations underscore the asymmetric thermoelectric behaviour

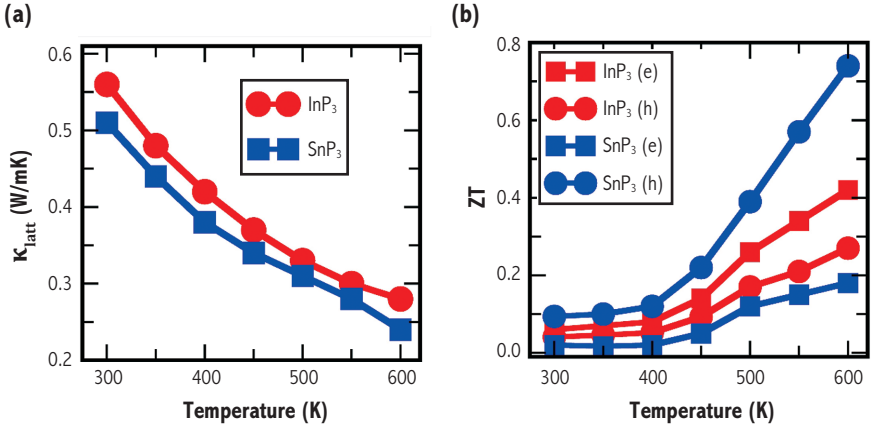

Figure 6 Calculated (a) lattice thermal conductivity and (b) figure of merit for the InP_3 and SnP_3 systems.

between electron and hole transport in monolayer triphosphides systems, which is governed by their unique electronic structures.

CONCLUSION

We have conducted a detailed comparative evaluation of monolayer InP_3 and SnP_3 to understand how structural and bonding variations influence their electronic and phonon transport characteristics. Both materials are dynamically stable and share the same trigonal lattice structure; however, Sn-P bonding is weaker and more flexible than In-P bonding, resulting in pronounced phonon softening, reduced Debye temperature, and lower lattice thermal conductivity in SnP_3. In contrast, InP_3 features steeper electronic band curvature and lower carrier effective mass, leading to significantly higher carrier mobility. The electrical conductivity of SnP_3 surpasses that of InP_3 due to its higher carrier concentration, while the enhanced density-of-states near the band edges leads to stronger Seebeck coefficients in InP_3. The combined effects yield higher *p*-type ZT in SnP_3 and superior *n*-type performance in InP_3. This comparative analysis demonstrates that metal change within the same structural family provides an effective route to engineer thermoelectric properties, enabling targeted design of high-performance 2D thermoelectric materials.

ACKNOWLEDGEMENTS

RKB acknowledges SERB-DST (EEQ/2022/000325) research grant for the financial support.

Author Declarations

Conflict of interest: The authors have no conflicts to disclose.

Data availability: The supporting data for the findings of this study can be found within the article.

REFERENCES

Backman, J., Lee, Y., & Luisier, M. (2024). Phonon-limited transport in two-dimensional materials: a unified approach for ab initio mobility and current calculations. *Physical Review Applied*, 21(5), 054017. https://doi.org/10.1103/PhysRevApplied.21.054017

Baroni, S., De Gironcoli, S., Corso, A.D., & Giannozzi, P. (2001). Phonons and related crystal properties from density-functional perturbation theory. *Reviews of modern Physics*, 73(2), 515. https:// doi.org/10.1103/RevModPhys.73.515

Deringer, V.L., Tchougréeff, A.L., & Dronskowski, R. (2011). Crystal orbital Hamilton population (COHP) analysis as projected from plane-wave basis sets. *The journal of physical chemistry A*, 115(21), 5461–5466. https://doi.org/10.1021/jp202489s

Dutta, M., Pal, K., Waghmare, U. V., & Biswas, K. (2019). 'Bonding heterogeneity and lone pair induced anharmonicity resulted in ultralow thermal conductivity and promising thermoelectric properties in n-type AgPbBiSe3'. *Chemical Science,* 10(18), 4905–4913.

Ghosh, B., Puri, S., Agarwal, A., & Bhowmick, S. (2018). SnP3: a previously unexplored two-dimensional material. *The Journal of Physical Chemistry C*, 122 (31), 18185–18191. https://doi.org/10.1021/acs.jpcc.8b06668

Giannozzi, P., Baroni, S., Bonini, N., Calandra, M., Car, R., Cavazzoni, C., Ceresoli, D., Chiarotti, G.L., Cococcioni, M., Dabo, I., Dal Corso, A., De Gironcoli, S., Fabris, S., Fratesi, G., Gebauer, R., Gerstmann, U., Gougoussis, C., Kokalj, A., Lazzeri, M., Martin-Samos, L., Marzari, N., Mauri, F., Mazzarello, R., Paolini, S., Pasquarello, A., Paulatto, L., Sbraccia, C., Scandolo, S., Sclauzero, G., Seitsonen, A.P., Smogunov, A., Umari, P., & Wentzcovitch, R.M. (2009). QUANTUM ESPRESSO: a modular and open-source software project for quantum simulations of materials. *Journal of physics: Condensed matter*, 21(39), 395502. 10.1088/0953-8984/21/39/395502

Gorczyca, I., Plesiewicz, J., Dmowski, L., Suski, T., Christensen, N.E., Svane, A., Gallinat, C.S., Koblmueller, G., & Speck, J.S. (2008). Electronic structure and effective masses of InN under pressure. *Journal of Applied Physics*, 104(1), 013704. https://doi.org/10.1063/1.2953094

Gullman, J. & Olofsson, O. (1972). The crystal structure of SnP3 and a note on the crystal structure of GeP3. *Journal of Solid State Chemistry*, 5(3), 441-445. https://doi.org/10.1016/0022-4596(72)90091-6

Jalil, A., Zhuo, Z., Sun, Z., Wu, F., Wang, C., & Wu, X. (2020). A phosphorene-like InP 3 monolayer: structure, stability, and catalytic properties toward the hydrogen evolution reaction. *Journal of Materials Chemistry A*, 8(3), 1307–1314. https://doi.org/10.1039/C9TA08612A

Jia, T., Chen, G., & Zhang, Y. (2017). Lattice thermal conductivity evaluated using elastic properties. *Physical Review B*, 95(15), 155206. https://doi.org/10.1103/PhysRevB.95.155206

Kinomura, N., Terao, K., Kikkawa, S., Horiuchi, H., Koizumi, M., & Setoguchi, H. (1983). Synthesis and crystal structure of InP3. *Materials Research Bulletin*, 18(1), 53-57. https://doi.org/10.1016/0025-5408(83)90171-X

Liu, J., Liu, C.S., Ye, X.J., & Yan, X.H. (2018). Monolayer InP 3 as a reversible anode material for ultrafast charging lithium- and sodium-ion batteries: a theoretical study. *Journal of Materials Chemistry A*, 6(8), 3634–3641. https://doi.org/10.1039/C7TA10248H

Madsen, G.K.H. & Singh, D.J. (2006). BoltzTraP. A code for calculating band-structure dependent quantities. *Computer Physics Communications*, 175 (1), 67–71. https://doi.org/10.1016/j.cpc.2006.03.007

Maintz, S., Deringer, V.L., Tchougréeff, A.L., & Dronskowski, R. (2016). LOBSTER: A tool to extract chemical bonding from plane-wave based DFT. *Journal of Computational Chemistry*, 37(11), 1030–1035. https://doi.org/10.1002/jcc.24300

Miao, N., Xu, B., Bristowe, N.C., Zhou, J., & Sun, Z. (2017). Tunable magnetism and extraordinary sunlight absorbance in indium triphosphide monolayer. *Journal of the American Chemical Society*, 139(32), 11125–11131. https://doi.org/10.1021/ jacs.7b05133

Mohanta, M.K., Rawat, A., Jena, N., Ahammed, R., & De Sarkar, A. (2020). Ultra-low lattice thermal conductivity and giant phonon-electric field coupling in hafnium dichalcogenide monolayers. *Journal of Physics: Condensed Matter*, 32(31), 315301. 10.1088/1361-648X/ab7e5f

Morelli, D.T., Heremans, J.P., & Slack, G.A. (2002). Estimation of the isotope effect on the lattice thermal conductivity of group IV and group III-V semiconductors. *Physical Review B*, 66(19), 1953041–1953049. https://doi.org/10.1103/PhysRevB.66.195304

Perdew, J.P., Burke, K., & Ernzerhof, M. (1996). Generalized gradient approximation made simple. *Physical review letters*, 77(18), 3865. https://doi. org/10.1103/PhysRevLett.77.3865

Perdew, J.P., Chevary, J.A., Vosko, S.H., Jackson, K.A., Pederson, M.R., Singh, D.J., & Fiolhais, C. (1992). Atoms, molecules, solids, and surfaces: Applications of the generalized gradient approximation for exchange and correlation. *Physical review B*, 46(11), 6671. https://doi.org/10.1103/PhysRevB.46.6671

Saeed, Y., Kachmar, A. & Carignano, M.A., (2017). First-principles study of the transport properties in bulk and monolayer MX3 (M= Ti, Zr, Hf and X= S, Se) compounds. *The Journal of Physical Chemistry C*, 121(3), 1399-1403. https://doi.org/10.1021/acs. jpcc.6b08067

Shuai, Z., Wang, L., & Song, C. (2012). *Deformation Potential Theory*. In Theory of charge transport in carbon electronic materials. Berlin, Heidelberg: Springer Berlin Heidelberg. 67–88.

Slack, G.A. (1973). Nonmetallic crystals with high thermal conductivity. *Journal of Physics and Chemistry of Solids*, 34(2), 321-335. https://doi.org/10.1016/0022-3697(73)90092-9

Sun, S., Meng, F., Wang, Hongyan, Wang, Hui, & Ni, Y. (2018). Novel two-dimensional semiconductor SnP 3: high stability, tunable bandgaps and high carrier Mobility Explored Using First-Principles Calculations. *Journal of Materials Chemistry A*, 6(25), 11890–11897. https://doi.org/10.1039/C8TA02494D

Sun, Z., Yuan, K., Chang, Z., Bi, S., Zhang, X., & Tang, D. (2020). Ultra-Low thermal conductivity and high thermoelectric performance of two-dimensional triphosphides (InP 3, GaP 3, SbP 3 and SnP 3): a comprehensive first-principles study. *Nanoscale,* 12(5), 3330–3342. https://doi.org/10.1039/C9NR08679J

Wang, Y., Wisesa, P., Balasubramanian, A., Dwaraknath, S., & Mueller, T. (2021). Rapid generation of optimal generalized Monkhorst-Pack grids. *Computational Materials Science*, 187, 110100. https://doi.org/10.1016/j.commatsci.2020.110100

Wu, H.H., Huang, H., Zhong, J., Yu, S., Zhang, Q., & Zeng, X.C. (2019). Monolayer triphosphates MP 3 (M = Sn, Ge) with excellent basal catalytic activity for hydrogen evolution reaction. *Nanoscale,* 11(25), 12210–12219. https://doi.org/10.1039/C9NR03255J

Yi, W., Chen, X., Wang, Z., Ding, Y., Yang, B., & Liu, X. (2019). A novel two-dimensional δ-InP 3 monolayer with high stability, tunable bandgap, high carrier mobility, and gas sensing of NO2. *Journal of Materials Chemistry C*, 7(24), 7352–7359. https://doi.org/10.1039/C9TC02030F

Zhang, S., Xie, Y., Hu, Y., Niu, X., & Wang, Y. (2018). Remarkable negative differential resistance and perfect spin-filtering effects of the indium triphosphide (InP 3) monolayer tuned by electric and optical Ways. *Physical Chemistry Chemical Physics*, 20(46), 29440–29445. https://doi.org/10.1039/C8CP05595E

Zhu, X.L., Liu, P. F., Zhang, J., Zhang, P., Zhou, W. X., Xie, G., & Wang, B. T. (2019). Monolayer SnP 3: An excellent p-type thermoelectric material. *Nanoscale*, 11(42), 19923–19932. https://doi.org/10.1039/C9NR04726C